Toward Predictive Permeabilities: Experimental Measurements and Multiscale Simulation of Methanol Transport in Nafion

Marielle Soniat[1,2], Sarah M. Dischinger[1,2], Lien-Chun Weng[1,3,4], Hajhayra Martinez Beltran[1,2,4], Adam Z. Weber[1,3], Daniel J. Miller[*,1,2], Frances A. Houle[*,1,2]

[1] Joint Center for Artificial Photosynthesis, Lawrence Berkeley National Laboratory, Berkeley, CA, 94720, USA

[2] Chemical Sciences Division, Lawrence Berkeley National Laboratory, Berkeley, CA, 94720, USA

[3] Energy Storage and Distributed Resources Division, Lawrence Berkeley National Laboratory, Berkeley, CA, 94720, USA

[4] Department of Chemical Engineering, University of California Berkeley, Berkeley, CA, 94720, USA

---

*Corresponding Authors

ABSTRACT

A polymer membrane's permeability to solutes determines its suitability for various applications: a permeability value is essential for predicting performance in diverse contexts. Using aqueous methanol permeation through Nafion as an example, we describe a methodology for determining membrane permeability that accounts for boundary layer effects and the possibility of swelling. For the materials and apparatus used herein, analysis of a permeance measurement and computational fluid dynamics simulations show that the mass transfer boundary layer is on the order of ones to tens of microns. The data are used to develop and validate a multiscale model describing solute permeation through a hydrated membrane as a series of physical mechanistic steps: reversible adsorption from solution at the membrane interface, diffusion driven by a concentration gradient within the membrane, and reversible desorption into solution at the opposite membrane interface. The validated model is used to predict methanol transport across a solar-driven CO_2 reduction device and to assess the impact of polymer changes on the measured value. The approach of combining experimental data, computational fluid dynamics, and the mechanistic multiscale model is expected to provide more accurate analysis of membrane permeation data in cases with polymer swelling or unusual device geometries, among others.

Keywords: membrane; permeability; experimental methods development; simulation; boundary layer

Table of Contents Figure (2 in. x 2 in.)

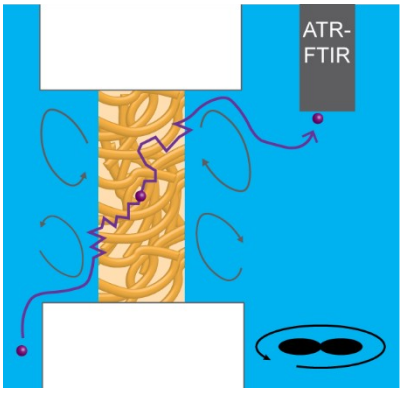

INTRODUCTION

Electrochemical devices such as batteries, fuel cells, and solar-driven CO_2 reduction devices constitute a critical portion of the developing alternative energy sector.[1–5] These devices produce or utilize electrical current when charge-carrying species move between physically separated electrodes.[6] The movement of other species (e.g., fuel molecules) between the electrodes, however, results in efficiency losses and compromised performance.[7–10] For example, if methanol in a direct methanol fuel cell crosses over from the anode to the cathode, it can be oxidized at the cathode, resulting not only in decreased fuel efficiency, but also in decreased cell voltage.[11]

Polymer electrolyte membranes (PEMs), which have charged functional groups tethered to the polymer backbone, are commonly employed in electrochemical devices to promote transport of charge-carrying electrolyte species while blocking products.[12–15] Electrochemical device performance depends greatly on the permeability of the PEM to various charged and neutral solutes.[7,11] The permeability quantifies solute transport in a membrane and is defined as the measured solute flux normalized by the membrane thickness and the driving force for transport.[16] Permeability is an intrinsic material property, dependent on the membrane chemistry and structure, the solute, and the solvent, and is independent of membrane thickness.[17] Determination of the permeability is key to the successful design of electrochemical systems, particularly under conditions that are far from steady-state or equilibrium. In this work we describe an experimental methodology for quantifying membrane permeability using methanol permeation through Nafion as an example system. Furthermore, we elucidate the mechanistic steps of methanol permeation through Nafion using a multiscale model and demonstrate the application of this model to electrochemical CO_2 reduction devices, an emerging energy technology.

The foundation of the method is the solution-diffusion model, a widely recognized continuum-level model of solute permeation through dense polymeric materials, including PEMs.[17–19] This model describes permeation of a solute across a membrane as a three-step process: 1) solute sorption into the membrane at the upstream interface, 2) solute diffusion across the membrane bulk, and 3) solute desorption from the membrane at the downstream interface.[17] The solution-diffusion model assumes that solute sorption and desorption at the membrane surface occur instantaneously such that the solute concentrations at the membrane surface and in the adjacent solution are in equilibrium.[17] Therefore, diffusion through the bulk of the membrane is the rate-limiting step. The permeability, P_m, of the membrane to a solute is:

$$P_m = K_m D_m \qquad \text{Eqn. 1}$$

where K_m is the solubility coefficient and D_m is the diffusion coefficient.[17] The solubility coefficient describes the equilibrium partitioning of a solute from the external solution into the membrane at the interfaces:

$$K_m = \frac{C_m^n}{C_s^n} \qquad \text{Eqn. 2}$$

where C_m^n is the equilibrium solute concentration in the membrane (subscript *m*) at the membrane-solution interface (superscript *n*), and C_s^n is the equilibrium solute concentration in the external solution

(subscript *s*). According to Fick's first law, the diffusion coefficient is the proportionality constant relating the diffusive mass flux, J, to the concentration gradient within the membrane, ∇C_m:[20]

$$J = D_m \nabla C_m \qquad \text{Eqn. 3}$$

under conditions of constant polymer properties (e.g., diffusion coefficient, polymer density) and constant temperature. The diffusivity describes the mobility of the solute in the membrane, and depends upon, among other factors, the segmental motion of the polymer chains, tortuosity of diffusive pathways, the solute size and shape, and the temperature.[21–25]

To verify the physical understanding of the solution-diffusion model, the three physical processes (i.e., sorption, diffusion, and desorption) were used herein to build a kinetic multiscale model of permeation. The advantage of a kinetic model is that the accuracy of its predictions are highly sensitive to steps being omitted from the mechanistic description of the permeation process. When all the mechanistic steps have been correctly identified and included, the kinetic model successfully predicts the experimentally-measured time-resolved concentration data resulting from solute permeation across a PEM, and reveals the key mechanistic elements. The goal of this type of modeling is to obtain a more detailed picture of the physical mechanisms of membrane permeation, in addition to the prediction of time-dependent downstream methanol concentration provided by the solution-diffusion model.

In previous work, we began development of such mechanistic permeation models using a multiscale simulation technique that included molecular-level detail for solute-polymer interactions and bulk-level transport within a single simulation framework. These mechanistic models have been used to successfully predict inert gas permeation through rubbers and also to account for time-varying polymer permeability in response to the presence of a solute.[26–28] We also developed a mechanistic model for methanol sorption into Nafion that suggested that the PEM experienced a morphological change in response to the presence of methanol.[28] By explicitly including this morphological change, our model was able to describe the experimental sorption data of Hallinan and Elabd[29] as well as add nuance to the interpretation of the data.

The development and validation of a multiscale model that predicts solute transport behavior over a wide range of conditions relies on accurate experimental permeability data. In the case of liquid transport through hydrated membranes, average permeabilities can be determined from simple diffusion cell experiments.[30–33] In these experiments, solutes diffuse across the membrane in response to a concentration gradient, and time-resolved concentration data are collected from the bulk solutions separated by the membrane. Solute concentrations in the bulk solutions can be measured by *ex situ* or *in situ* analytical techniques. While *ex situ* techniques (e.g., gas, ion, or high performance liquid chromatography, nuclear magnetic resonance spectroscopy, total organic carbon analysis) offer high resolution and chemical specificity, isolating samples from the experimental apparatus *in operando* is laborious and restricts the number of samples that can be collected before significantly affecting the liquid volume in the diffusion cells.[34–37] In contrast, *in situ* conductivity or spectroscopy probes rapidly collect concentration measurements with minimal disruption to the experimental system.[32,33,38,39] Conductivity measurements only detect the presence of charged species and generally lack chemical specificity. Ultraviolet, visible, and infrared spectroscopy, however, offer chemical specificity for organic species. Submergible UV-vis and IR spectroscopic probes can be used to monitor changes in solution composition *in situ* over time.[32,38,39] Implementing such technologies in liquid permeation experiments has enabled high-sensitivity collection of time-resolved concentration data from which membrane permeabilities can be calculated.[32]

In this work, we have carried out a rigorous set of time-resolved experiments of methanol permeation through Nafion using a diffusion cell and have developed a mechanistic multiscale model. From the experimental data, we identify the presence of mass transport boundary layers and calculate membrane permeability. We confirm the experimentally calculated mass transfer boundary layer thickness using computational fluid dynamics. Careful analysis of experimental results allow us to calculate membrane permeability independent of the experimental conditions and enable validation of the multiscale model. Once validated, the multiscale model of permeation can be used to predict methanol transport under a variety of conditions; one condition that we explore is methanol transport through a solar-driven CO_2 reduction device. The mechanistic multiscale model adds to our understanding of permeability by confirming that the continuum-level picture of the solution-diffusion model applies in the specific case studied, while emphasizing that adsorption and desorption at the interfaces must be reversible mechanistic steps under non-steady state conditions. The methodology we have developed is expected to be broadly applicable to other membrane-permeant systems.

Calculating Permeability from Experimental Data

For permeation experiments in diffusion cells, in which a concentration gradient is the only driving force for solute transport, mass fluxes are described by Eqn. 3. For membrane applications, the concentration gradient of Eqn. 3 is the difference between the solute concentrations within the polymer, C_m^n, at the upstream and downstream membrane interfaces. However, because it is challenging to explicitly measure the concentration at the membrane-solution interface during diffusion cell experiments, the bulk solution concentration is measured instead. Under the assumption that the concentration in the bulk solution is equal to the solution concentration at the membrane interface, the solubility coefficient from Eqn. 2 is used to convert Eqn. 3 into an experimentally tractable relationship:

$$J = \frac{D_m K_m}{\delta_m}\left(C_s^{b,u} - C_s^{b,d}\right) \qquad \text{Eqn. 4}$$

where δ_m is the thickness of the membrane, and $C_s^{b,u}$ and $C_s^{b,d}$ are the upstream (superscript *u*) and downstream (superscript *d*) concentrations in the bulk (superscript *b*) solutions. Applying the solution-diffusion model of Eqn. 1 gives:[16]

$$J = \frac{P_m}{\delta_m}\left(C_s^{b,u} - C_s^{b,d}\right) \qquad \text{Eqn. 5}$$

Flux through a membrane can also be written as:

$$J = \frac{dC_s^{b,d}}{dt}\frac{V^d}{A} \qquad \text{Eqn. 6}$$

where t is time, V^d is the downstream volume, and A is the area available for solute transport. To obtain an analytical solution for flux within a closed system, Eqn. 5 and 6 are combined and integrated with respect to time. In typical experimental setups, the active area available for transport and the liquid volume on either side are constant with time. With an initial downstream concentration of zero and equal liquid volumes on both sides of the membrane, an expression for the time-resolved downstream solution concentration ($C_s^{b,d}[t]$) is obtained:

$$ln\left(1-\frac{2C_s^{b,d}[t]}{C_s^{b,u}[0]}\right)=\frac{-2P_mA}{\delta_mV}t \qquad \text{Eqn. 7}$$

where $C_s^{b,u}[0]$ is the upstream bulk solution concentration at $t=0$. Eqn. 7 can be fitted to experimental downstream concentration data, $C_s^{b,d}[t]$, using P_m as a fitting parameter.[30–33] P_m is the time- and space-average permeability of the region between the two bulk solutions on the upstream and downstream solutions, and equals the membrane permeability only when the following conditions are true:

(i) the membrane thickness is constant with time
(ii) the solution concentration at the membrane surface is the same as in the bulk [40]
(iii) the membrane permeability is constant with time

While it is straightforward to determine whether swelling occurs (condition (i)), and whether permeability is constant, condition (iii), it is very challenging to measure the solute concentration at the membrane surface in order to evaluate whether condition (ii) is met. It is important to note that the time dependence of Eqn. 7 enables comparison with the transient multiscale model; systems in which transient behavior is not expected could be modeled with a simpler approach.[41,42] An alternative approach using the same set of time-resolved downstream concentration data facilitates the calculation of permeability *via* determination of permeance without requiring measurement of the concentration at the membrane interface. By considering the membrane and any regions between the membrane and the bulk solution as a series of resistances to mass transport, the total resistance between the two bulk solution regions is expressed as:[43]

$$R_{tot}=2R_{BL}+R_m \qquad \text{Eqn. 8}$$

where R_{tot} is the total resistance, R_{BL} is the resistance in the solution-phase boundary layers on either side of the membrane, which control the concentration of solutes available at the interface, and R_m is the resistance of the membrane. Eqn. 8 assumes that the resistance due to the boundary layer is the same on both the upstream and downstream sides of the membrane, which is reasonable because the stirring speed, stir bar, cell geometry, and fluid volume was the same in both chambers. It is important to note that the boundary layers represent resistance to mass transport between the bulk solution and the membrane interface and do not necessarily correlate with concentration gradients at the membrane surface, as referred to in condition (ii). Boundary layers will be discussed further in the CFD methods section. Because of the geometry of the diffusion cell, we assume that this boundary layer thickness is the same on either side of the membrane and is independent of the membrane thickness and permeability.[40] The permeance, $\mathbb{P}$, describes the solute flux from the bulk solution in the upstream cell to the bulk solution in the downstream cell, a transport path across both the boundary layers, the membrane-solution interfaces, and the membrane, and is calculated as:[43]

$$\mathbb{P}=\frac{dC_s^{b,d}}{dt}\frac{V^d}{A}\frac{1}{\left(C_s^{b,u}-C_s^{b,d}\right)}=\frac{J}{\left(C_s^{b,u}-C_s^{b,d}\right)} \qquad \text{Eqn. 9}$$

Permeance differs from permeability by a factor of the characteristic distance between the bulk upstream and downstream solutions (this distance includes the membrane thickness and the thickness of any boundary layers that are present between the membrane-solution interface and the bulk solution), and can be calculated directly from experimental conditions without defining this characteristic distance.

Permeance is related to the total resistance between the bulk solutions in the upstream and downstream cells by:[43]

$$\mathbb{P} = \frac{1}{R_{tot}} = \frac{D_m D_w K_m}{D_m K_m 2\delta_{BL} + D_w \delta_m} \quad \text{Eqn. 10}$$

where D_w is the diffusion coefficient of methanol in water, (1.27×10^{-5}) cm^2/s,[44] and δ_{BL} is the thickness of the mass transfer boundary layer. The membrane-solution interface is assumed to have zero thickness. Eqn. 10 has two unknowns, D_m and δ_{BL}, both of which are assumed to be independent of the membrane thickness. Therefore, by measuring $\mathbb{P}$ for two different values of δ_m, a system of two equations and two unknowns can be solved to calculate δ_{BL}:

$$\delta_{BL} = \frac{D_w}{2} \frac{\frac{\delta_{m1}}{\mathbb{P}_2} - \frac{\delta_{m2}}{\mathbb{P}_1}}{\delta_{m,1} - \delta_{m,2}} \quad \text{Eqn. 11}$$

where the subscript 1 indicates the δ_m and corresponding $\mathbb{P}$ for one experiment and subscript 2 indicates the δ_m and corresponding $\mathbb{P}$ for the other experiment.[40,41] Once the thickness of the boundary layer is known, the diffusion coefficient of the membrane can be calculated from a rearrangement of Eqn. 10:

$$D_m = \frac{\mathbb{P} D_w \delta_m}{D_w K_m - \mathbb{P} K_m 2\delta_{BL}} \quad \text{Eqn. 12}$$

The membrane's permeability can then be calculated from the diffusion coefficient and solubility coefficient, as shown in Eqn. 1. While this approach is used less often in the literature because it requires two membranes of different thicknesses, it enables the presence of any mass transfer boundary layers to be assessed, and yields a membrane permeability of increased accuracy because fewer assumptions are required.

METHODS

Experimental

Materials

Nafion R-1100 was purchased from Alfa Aesar. Nafion 117 was purchased from the Fuel Cell Store. Dimethyl sulfoxide (DMSO), methanol, and nitric acid were purchased from Sigma Aldrich. Potassium hydroxide (KOH) was purchased from VWR International. All reagents were used as received. Deionized (DI) water was collected from an EMD Millipore Milli-Q Integral 3 water purification system (18.2 MΩ cm at 25 °C, 1.2 ppb TOC).

Activation of Nafion R-1100 to Nafion 1100

Nafion R-1100 is a ca. 50 μm thick film of perfluorinated precursor resin in the sulfonyl fluoride form.[45] As received, this membrane does not have ionic functional groups; the sulfonyl fluoride groups must be hydrolyzed in order to convert this membrane into a polymer electrolyte membrane. This membrane was chosen because it was thinnest commercially available option with the same equivalent weight (EW) as the widely studied Nafion 117 membrane. The chemical conversion of the membrane resin was done per the manufacturer's instructions by first rinsing the membrane in DI water and then submerging it in a bath of 50 wt% water, 35 wt% DMSO, and 15 wt% KOH at 80 °C for about 1 h.[45] The membrane was then removed, rinsed with fresh DI, and submerged in a bath of fresh DI water at room temperature. The DI water was exchanged four times over a period of 6 h to remove any trace of DMSO or KOH from the previous soak. The membrane was then submerged in 12 wt% nitric acid at room temperature.[45] The nitric acid solution was replaced three times over a period of about 36 h. The membrane was then rinsed with DI water and moved to a bath of fresh DI water at room temperature. The DI water was exchanged once over a period of 36 h. The membrane was then stored sealed in fresh DI water. The activated Nafion R-1100 membrane in its acidic form, post 36-h DI soak, will be referred to as Nafion 1100 throughout the remainder of this work.

Nafion 117, used as a control for sorption experiments, was pretreated by soaking as-received membranes in 3 wt% H_2O_2 at 80 °C for 2 h. The membrane was then rinsed with fresh DI water and subsequently submerged in DI water at 80 °C for 2 h. The membrane was submerged in 0.5 M H_2SO_4 at 80 °C for 1 h. The membrane was removed, rinsed with fresh DI water, and submerged in DI water at 80 °C for 1 h.[46] The Nafion 117 membrane was then removed and stored in fresh DI water until use.

Methanol Sorption

Methanol sorption was measured using a previously published desorption technique that is summarized here.[47] Nafion 1100 discs 1.5 cm in diameter were soaked in 30 mL DI water for 2 days, replacing the DI water with fresh DI water every 24 h, to remove any trace contaminants. The thickness of each membrane was measured at multiple locations using a micrometer. Each membrane sample was then removed from the water, blotted to remove any excess water from the surface, and submerged in 30 mL of 1 M aqueous methanol solution. After 3 days of soaking in the methanol solution, membrane thicknesses and diameters were measured. Then each membrane was removed from its soak solution, blotted to remove any excess solution from the surface, and submerged in 5 mL of DI water. After 3 days, each membrane was moved into a fresh 5 mL of DI water as a second desorption step. The amount of methanol in each desorption solution was quantified using ^{1}H nuclear magnetic resonance spectroscopy (Bruker Ascend 500).[34] The same procedure was used for Nafion 117 samples. The concentrations measured herein were equilibrium concentrations, and the concentrations in the bulk and at the interface within each phase were assumed to be equal. The solubility coefficient of methanol in Nafion was calculated using Eqn. 2.

Water Sorption

The mass of fully hydrated Nafion 1100 samples was measured after blotting the membrane surface to remove any excess water. The samples were then dried under atmosphere at room temperature for 6 h and then dried under vacuum (<1 Torr) at 40 °C until reaching a constant dry weight. The mass of each dried membrane was measured immediately after it was removed from the vacuum so as to minimize the effect of water uptake from ambient air.

Methanol Permeation Experiments

Nafion 1100 samples were first soaked in fresh DI water for at least 8 h to remove any contaminants. Degassed DI water was prepared by stirring the water rapidly at 40 °C until no gas bubbles remained. The water was then moved to a vacuum oven chamber at 40 °C, and vacuum (<1 Torr) was applied for about 30 s. The pressure inside the chamber was then slowly increased to atmospheric pressure at 40 °C. The water was removed from the vacuum oven chamber and quickly sealed, and allowed to cool to room temperature. The same method was used to degas methanol.

Figure 1 shows a photograph (a) and a dimensional diagram (b) of the diffusion cell experimental apparatus (Adams and Chittenden Scientific Glass, Berkeley, CA). The initial thickness of the membrane was measured with a micrometer while maintaining the hydration of the membrane by returning it intermittently to DI water. Membrane samples were placed between silicone gaskets with an inner diameter matching that of the apertures in diffusion cell halves, resulting in an area available for solute transport of 1.77 cm^2. The gasket-membrane sandwich was assembled into the diffusion cell. 30 mL of degassed DI water was added to the downstream cell and 29.2 mL of degassed DI water was added to the upstream cell. The diffusion cell was jacketed, and the temperature of the recirculating water was (25 ± 1) °C. Each cell was stirred with a magnetic stir bar at 600 rpm. An *in situ* ATR-FTIR probe (Mettler-Toledo ReactIR 15 with a shallow tip 9.5 mm DSun AgX DiComp probe) was inserted into each cell after having collected a background (air) spectrum.

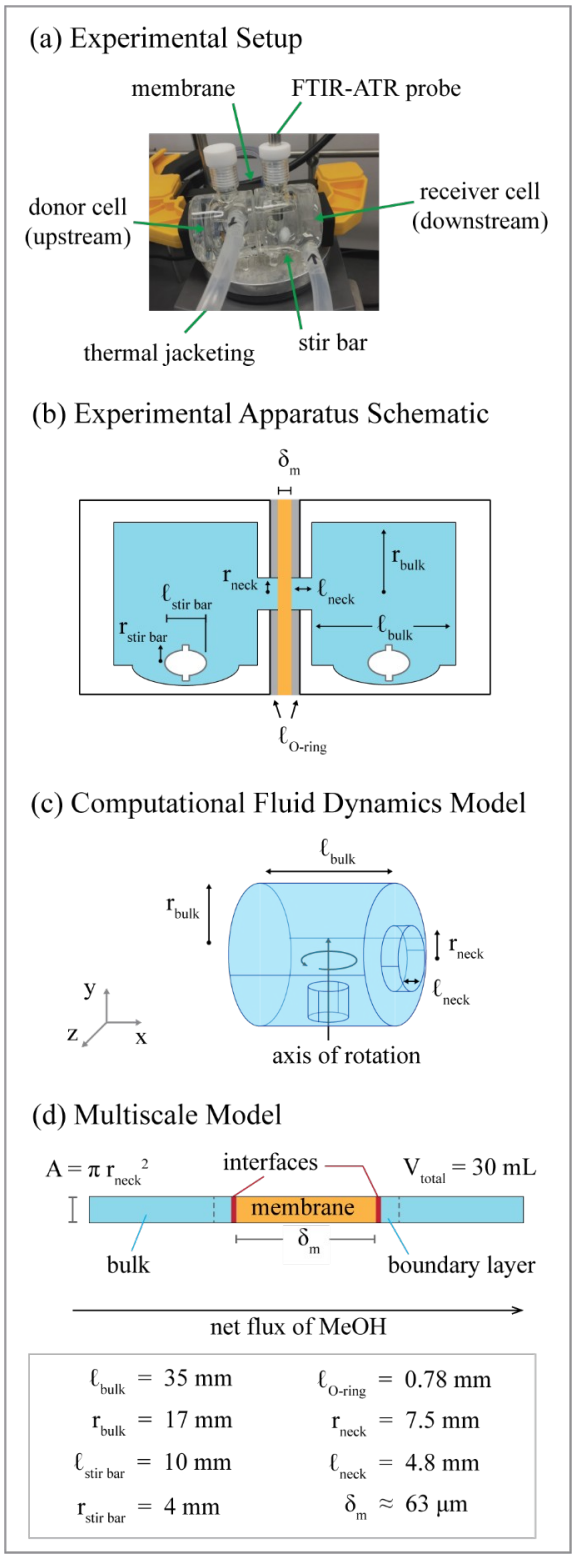

Figure 1. The (a) experimental setup (showing one FTIR probe, experiments were also conducted with FTIR probes in both upstream and downstream cells) and (b) experimental apparatus schematic are used to determine the geometry of the (c) cell in the CFD simulation and the (d) multiscale model. Relevant dimensions are shown at the bottom of the Figure.

After degassed DI water was added to each cell, three IR spectra (3000 cm^{-1} to 640 cm^{-1}) were collected before ca. 0.9 g degassed methanol was added directly to the upstream cell, resulting in an upstream concentration of 1 M methanol. A new spectrum was collected every minute until the methanol concentrations in both cells equalized, about 3 days. Even the spectrum collected from the downstream side directly after the methanol addition to the upstream side showed some trace of methanol above the baseline, suggesting that the lag-time for permeation was shorter than the 1-minute resolution of the spectrum collection. This observation agrees with the characteristic timescale for diffusion[48] (see SI pg 5) which suggests that methanol diffuses across the membrane in about 7 s. These experiments were run to equilibrium in order to evaluate the permeability over time and to enable an accurate mass balance. Every 8-12 h, the probes were removed from the diffusion cell and cleaned. A fresh background in air and a degassed DI water spectrum were collected before returning the probes to the diffusion cell to continue collecting spectra.

The spectral data were collected and analyzed using iC IR 7.1 software (Mettler-Toledo). Each spectrum collected by the ATR-FTIR probes was an average of 256 scans. A degassed DI water spectrum was subtracted from each sample spectrum to eliminate the infrared absorbance of water. The baseline of each spectrum was corrected by setting the value at 1200 cm^{-1}, a wavenumber within the featureless region of the spectrum, to zero. The peak height at 1018 cm^{-1}, corresponding to the C-O bond stretching vibration of methanol,[49] was measured with respect to a two-point baseline from 1243-1187 cm^{-1}, a wavenumber range which also falls within the featureless region of the spectrum. The peak height was converted to methanol concentration using a calibration curve (see Fig. S1 of the SI). Time-resolved concentration data for both the downstream and upstream cells were converted to total mass to ensure closure of a methanol mass balance over the diffusion cell.

Method Development for Permeation Experiments

The above procedure for permeation experiments was the result of a rigorous approach to assess the accuracy of the time-resolved concentration profiles. This approach utilized concentration measurements of methanol on both the upstream and downstream sides of the membrane to conduct a mass balance across the diffusion cell using the spectroscopic data. Explicit measurement of the initial masses of methanol and water added were used instead of volume measurements because mass measurements provided greater accuracy. Using the methods described in this section, we confirmed that the final mass of methanol detected was within error of the initial mass of methanol added.

Collecting time-resolved concentration data with high accuracy for prolonged periods using *in situ* ATR-FTIR requires an assessment of instrument stability beyond the 8 min stability test implemented by the manufacturer-provided software.[50] The stability of the instruments was evaluated by submerging the probes in a sealed container of DI water and tracking the signal height at 1018 cm^{-1}, the infrared absorption used to detect methanol. Over a 42 h period, an increase in the signal height was observed corresponding to an apparent concentration increase greater than 0.01 M methanol, which is much greater than the 0.002 M signal variation error observed during the standard calibration method. While a 0.01 M variation may be considered negligible in many applications, it can be significant when the experimental data are being used to validate a modeling study, and a full mass balance in the system is being tracked. The time-resolved data could not be corrected using a general long-term calibration since the rate of drift was not reproducible across multiple stability assessment runs.

Two adjustments to the method were found to mitigate the observed drift in signal height. The first change relates to the calculation of the signal peak height, which is the difference between the signal at

1018 cm^{-1} and a reference point within the spectrum. The region of interest for selecting a reference point internal to the spectrum was the featureless region between 1300 cm^{-1} and 1150 cm^{-1}. A two-point baseline defined by 1243 cm^{-1} and 1187 cm^{-1} was chosen because the resulting 1018 cm^{-1} signal peak height demonstrated no net drift over 42 h (Fig. S2 of the SI). In contrast, the same signal peak height calculated from a single-point baseline located at 1200 cm^{-1} did demonstrate observable drift over 42 h (Fig. S2). The second adjustment to the method relates to the instrumentation itself. The signal peak height drift was further mitigated by the collection of new background spectra throughout the duration of the experiment. This was necessary because FTIR instruments drift in response to environmental temperature fluctuations.[51] Even though the experiments conducted herein employed best practices in temperature control by submersing the probe tip into a jacketed diffusion cell and by maintaining a liquid nitrogen reservoir to control the temperature of the instrument electronics, signal drift over experimental durations exceeding 1.5 h was still observed. The drift was mitigated by collecting new background spectra during the course of the experiment.[51] The impact of collecting a new background is shown in Fig. S3 of the SI, in which the signal peak height of a static solution returns to its original value after the collection of a new background. During permeation experiments, a new background was collected every 8-12 h to identify the drift occurring and mitigate the effect of drift on the mass balance.

Degassing the DI water and methanol before addition to the system was necessary to close the mass balance on methanol because the accuracy of the FTIR-ATR measurements was severely compromised by the formation of gas bubbles. Upon the addition of air-saturated DI water and air-saturated methanol to the system, gas bubbles formed in the upstream cell. The bubbles formed because the resultant 1 M aqueous solution had an oxygen mole fraction 23% greater than its saturation concentration in this mixture.[52] These air bubbles became entrained on the ATR-FTIR probe, blocking a portion of the sensor's active area and causing a rapid decrease in the apparent total mass of methanol within the system. The apparent total mass of methanol in the system would then slowly increase over about 200-400 min, as the system re-equilibrated with the atmosphere. Degassing both the water and the methanol before their addition to the diffusion cell significantly reduced the formation of gas bubbles.

By incorporating a two-point baseline in the data analsysis, frequent collections of new backgrounds throughout the experiment, and degassed solutions, the mass balance of the system over the duration of the experiment was brought within a reasonable level (0.005 g methanol), close to the sensitivity limit of the instrument for methanol of 0.004 g in a 60 mL volume of solution. (Fig. S4 of the SI). A closed mass balance supports confidence in the accuracy of the time-resolved downstream concentration profile.

Mass Transfer Boundary Layer and Methanol Permeability from Experiment

When the concentration boundary layer cannot be measured to evaluate condition (ii) associated with Eqn. 7, the membrane permeability can be calculated by determining the mass transfer boundary layer thickness by comparison of permeance of membranes of differing thicknesses. Membrane thickness, δ_m, is an independent variable in the calculation of permeance (Eqn. 10) that can easily be controlled and measured. By varying the membrane thickness rather than the boundary layer thickness (by way of varying the stirring speed or viscosity in the bulk solution), the unknown terms of Eqn. 10 are constant even with variation in membrane thickness, enabling one to solve a system of two equations with two unknown values (leading to Eqn. 11). In the present work, the mass transfer boundary layer thickness was calculated from membrane permeances of single and double membrane thicknesses. Data from single-membrane thickness (ca. 64 μm) experiments were collected from the permeation experiments described in the previous section. Double-membrane thickness (ca. 128 μm) was achieved by stacking two Nafion

1100 samples together while submerged in DI water to prevent air bubbles from being captured between the membranes. Double-membrane thickness permeation experiments were conducted in a manner similar to the single-membrane thickness experiments. However, because the aim of the double-membrane thickness experiments was to collect enough data for the permeance calculations, the downstream concentration was measured with ATR-FTIR for the first 12 h; degassed solutions were not necessary because the upstream concentration was not monitored. Throughout the duration of the experiments, the flux decreased as the concentration difference between the upstream and downstream cells decreased. Therefore, the permeance was calculated from experimental data as a rolling average of 19 consecutive time points collected one minute apart.

Three permeation experiments with a membrane thickness ca. 64 μm and two permeation experiments with a membrane thickness ca. 128 μm were conducted. An average permeance was calculated for each membrane thickness, and these values were used in Eqn. 11 to calculate an average boundary layer thickness. The standard deviations between multiple experiments of the same membrane thickness were propagated to determine the error in the boundary layer thickness value.[53] The diffusion coefficient was then calculated from Eqn. 12, and the permeability from Eqn. 1. The standard deviation was propagated throughout these calculations.

Membrane permeability was also calculated by fitting the time-resolved downstream concentration data from single-membrane thickness experiments to Eqn. 7 using P_m as a fitting parameter with $C_s^{b,d}[0]$, V, and δ_m collected from the relevant experimental conditions. Thus, the uncertainty reported represents one standard deviation due to variation between different replicate samples.

Computational Fluid Dynamics

Computational fluid dynamics simulations were used to calculate the mass transfer boundary layer thickness for comparison to the values extracted from the permeance measurements. The solution velocity and concentration profiles in the upstream cell were modeled using the COMSOL Multiphysics® software.[54] The experimental apparatus is treated as a set of cylinders with dimensions equal to those measured from the diffusion cell (see Fig. 1c). The other model inputs are summarized in Table S3 of the SI.

A Reynolds-averaged Navier-Stokes model is used to determine the velocity profile, $\mathbf{u}$. The fluid is assumed to be incompressible and Newtonian. The governing equations are the continuity equation:

$$\rho \nabla \cdot \mathbf{u} = 0 \qquad \text{Eqn. 13}$$

and the Navier-Stokes equation:

$$\rho(\mathbf{u} \cdot \nabla)\mathbf{u} = \nabla \cdot \left[-p\mathbf{I} + \mu\left(\nabla\mathbf{u} + (\nabla\mathbf{u})^{\mathrm{T}}\right)\right] \qquad \text{Eqn. 14}$$

where ρ and μ are the density and the dynamic viscosity of the fluid, p is the pressure, and $\mathbf{I}$ is the identity matrix. The κ-ε turbulence model is chosen to simulate turbulent flow because of its low computational cost.[55] The stir bar is treated as a rotating cylinder with a rotation speed of 600 min^{-1}. A no-slip condition is applied to all wall surfaces and the membrane.

The location-dependent concentration of methanol on the upstream side, $\mathbb{C}_s^u$, is calculated using a molar balance:

$$\nabla \cdot \mathbf{J} + \mathbf{u} \cdot \nabla \mathbb{C}_s^u = 0 \qquad \text{Eqn. 15}$$

where the $\mathbf{J}$ is the diffusive flux, calculated as the product of the diffusivity of methanol in water, D_w, and its concentration gradient:

$$\mathbf{J} = -D_w \nabla \mathbb{C}_s^u \qquad \text{Eqn. 16}$$

The total flux of methanol through the membrane surface (flux boundary condition) is:

$$\mathrm{J}_s^{n,u} = -\frac{D_m K_\mathrm{m}}{\delta_m}\left(2\mathbb{C}_s^u - \mathbb{C}_s^u[0]\right) \qquad \text{Eqn. 17}$$

where $\mathbb{C}_s^u[0]$ is the location-dependent methanol concentration on the upstream side when $t = 0$. A no-flux condition is applied to all other wall surfaces. The velocity profile is first calculated from Eqn. 14 and then used in Eqn. 15 to calculate the concentration profile. Using the calculated concentration profile, average upstream bulk concentration (excluding the neck region), $\overline{\mathbb{C}_s^{b,u}}$, and the average methanol concentration at the membrane interface, $\mathbb{C}_s^{n,u}$, were calculated.

For continuum-level simulations, it is convenient to assume that the change from average bulk concentration to average surface concentration is due to diffusive flux through a stagnant layer of solution. This stagnant layer is defined as the mass transfer boundary layer, which has a thickness, δ_{BL}, of

$$\delta_{BL} = \frac{1}{A}\int_A \frac{D_w}{\mathrm{J}_s^{n,u}}\left(\overline{\mathbb{C}_s^{b,u}} - \overline{\mathbb{C}_s^{n,u}}\right) dA \qquad \text{Eqn. 18}$$

Note that the mass transfer boundary layer is an idealized concept, since a sharp division between a well-mixed bulk and a stagnant boundary layer is not physically possible within a fluid. The concentration and hydrodynamic profiles both contribute to the mass transfer boundary layer but not in a straightforward manner. In addition, the concentration and hydrodynamic boundary layers, which are typically defined as the region in which concentration or velocity, respectively, is less than 99% of the bulk values,[56] may have very different thicknesses from the mass transfer boundary layer. The different types of boundary layers are examined further in the Discussion section.

Multiscale Modeling

Model-Building Approach

The multiscale model building in this work used an inductive approach in which the simplest possible description was tested first, and then complexity was added only if the simple model did not agree with experimental data. This type of model building has been used to discover aspects of the underlying physics and chemistry that determine the observed experimental behavior,[57] i.e., it established a mechanistic model. In addition, this model was a kinetic model, meaning that reaction and diffusion steps

defined the permeation process. Specifically, the steps were that (1) the solute transited from the bulk upstream solution to the membrane surface, (2) sorbed into the membrane, (3) diffused through the membrane, (4) desorbed from the membrane, and (5) transited from the membrane surface into the downstream bulk solution. Reaction and diffusion coefficients were not adjustable parameters; they were extracted from measurements. Starting from the experiment's initial methanol concentration and membrane geometry, the simulations generated concentration vs time data for both the upstream and downstream regions of the cells for direct comparison to experimental data. The kinetic model was validated when the predicted downstream methanol concentration agreed with experiment at all time points. If there was qualitative or quantitative disagreement, the model was used to identify which steps were involved. More detail on the reaction and diffusion steps is given below; the 1-dimensional representation of the system, similar to previous permeation studies, is summarized in Figure 1d.[26–28]

The system was divided into several regions: the bulk solution, the boundary layers, the membrane, and the interfaces between the boundary layer and membrane regions. This framework was multiscale because it depicted different regions of the experimental system with different resolutions, e.g. micrometers within the membrane and centimeters for the bulk aqueous regions. Both the solution and membrane regions were sub-divided into multiple compartments in order to minimize computational distortions from artificially large gradients, as discussed in section 3 of the SI. Bidirectional diffusion was included, with forward and reverse rates depending on local, time-dependent concentration gradients.

The average value of the boundary layer thickness determined from measurements was used, δ_{BL} = 4 μm. The values for δ_m, D_m, and $C_s^{b,d}[0]$ used in the simulations presented in the main text are from a single experiment (see Table S2 Experiment ID 2SD58 in the SI); simulations of additional experiments are reported in SI Section 2.

Treatment of Bulk Solution Regions

The volumes of the bulk solution regions were 30 mL and assumed to have the same cross-sectional area as the membrane area A. This representation of the bulk solution geometry had a different aspect ratio than the geometry in the diffusion cell, but because the solution was rapidly stirred in both the experiment and the simulation, the bulk solution form factor did not affect the simulation results. The bulk solution regions were divided into 10 equally-sized compartments; sensitivity to the description of the compartments was tested and reported in the Section 3 of the SI. In the upstream cell, the initial upstream bulk methanol concentration, $C_s^{b,u}[0]$, was 0.97 M and the initial downstream methanol concentration, $C_s^{b,d}[0]$, was 0 M. The bulk solution regions are considered well mixed, so the diffusion coefficient between the compartments is set to an arbitrarily large value of (1×10^{-4}) m^2/s; this value resulted in all compartments within the bulk solution region having the same methanol concentration within 60 s, equal to the sampling rate of the FTIR-ATR probe. Increasing the diffusion coefficient further to increase the rate of mixing within the bulk reduced the computational efficiency of the simulation; this value was found to be the best compromise between mixing rate and computational efficiency.

Treatment of Boundary Layer

The mass transfer boundary layer was calculated from measurements in the present work to have a thickness of 4 μm. On both sides of the membrane, the boundary layer was considered to be a stagnant

layer of water, which was divided into 10 equally-sized compartments. Within stagnant water, methanol had a diffusion coefficient D_w = (1.268 × 10^{-9}) m^2/s.[44] Due to the large uncertainty in the mass transfer boundary layer thickness calculation, additional simulations with other boundary layer thicknesses were performed; these are listed in Table 1 together with the corresponding diffusion coefficients, D_m, calculated from the permeance (Eqn. 12).

Table 1. List of multiscale simulations.

Simulation	δ_{BL} μm	D_m cm^2/s
1	0	5.13 × 10^{-6}
2	4	5.21 × 10^{-6}
3	10	5.34 × 10^{-6}
4	30	5.82 × 10^{-6}
5	50	6.41 × 10^{-6}
2s [a]	4	5.21 × 10^{-6}

[a] includes swelling

Treatment of Membrane Bulk

The 63.3-μm thick membrane was divided into 100 compartments of equal thickness; previous work has shown that compartment sizes of 1 μm or less did not suffer from compartment size artifacts.[26] Within the membrane, methanol diffused as driven by its instantaneous concentration gradient. The cross sectional area of each compartment, which controls the diffusion rate and hence the flux, was 1.767 cm^2. No swelling of the membrane was observed experimentally, and so swelling was also neglected within the simulations presented within the main text.

However, swelling of Nafion when in contact with methanol has been observed in many studies[29,58,59] and was determined to be a rate-limiting step in our previous work on methanol sorption into Nafion.[28] Therefore, an additional simulation in which the impact of swelling is explored was carried out. The methods for including swelling were developed in our previous work[28] and are summarized in the SI Section 3 along with our findings. A brief overview of the outcomes is presented in the Results Section below.

Treatment of Solution-Membrane Interfaces

The first and final membrane compartments were treated as the interfaces between the membrane and the solution within the boundary layer. The adsorption and desorption of methanol at the interfaces were implemented as a reversible physical reaction:

$$MeOH_{(aq)} \underset{k_r}{\overset{k_f}{\longleftrightarrow}} MeOH_{(p)} \qquad \text{Eqn. 19}$$

where methanol in the aqueous phase, $MeOH_{(aq)}$, binds to the polymer membrane at the liquid-polymer interface, $MeOH_{(p)}$, in the forward reaction and is released in the reverse reaction. The full sorption process combines the interfacial adsorption and subsequent diffusion steps.

No rate coefficients have been measured for the reaction in Eqn. 19; therefore they were estimated as follows. Typically, diffusion-controlled reactions of small molecules within water have rate coefficients on the order of 10^9 M^{-1} s^{-1} for a bimolecular reaction[60], and so can be considered an upper limit for the interfacial adsorption reaction. This coefficient was converted to a pseudo-first order rate coefficient by assuming that the available binding site within the polymer had a concentration equal to $K_m C_s^b$, which gave an upper limit for the rate coefficient of the order of 10^8 s^{-1}. However, implementation of such a large rate coefficient for a reversible reaction was computationally expensive. Therefore, the value of the forward rate coefficient, k_f, was systematically reduced until a value of (1×10^3) s^{-1} was found to be computationally feasible without a loss in accuracy of the predicted permeation process (shown in Fig. S10 of the SI). The reverse (desorption) rate coefficient, k_r, was calculated based on the equilibrium condition

$$k_f C_s^n = k_r C_m^n \qquad \text{Eqn. 20}$$

where

$$K_m = \frac{C_m}{C_s} = \frac{k_f}{k_r} \qquad \text{Eqn. 21}$$

to give a value of (3.23×10^3) s^{-1} using K_m in Table 2.

Numerical Procedure

The system of reaction and diffusion steps was simulated using the open access package Kinetiscope, which implements a stochastic algorithm (SA) that is a type of Kinetic Monte Carlo and is explained in Section 4 of the SI.[61–64] The SA is a rigorous solution to the master equation for Markov systems that can properly describe swelling, development of non-Fickian diffusion, and other dynamic changes to material properties, permitting a more general representation of permeation than is possible with differential equation solvers.[28,63,65]

RESULTS

Experiment

Nafion 1100 Membrane Properties

Nafion 1100 is a commercial cation exchange membrane with an equivalent weight of 1100 g polymer/mol of sulfonic acid groups (the same as Nafion 117, according to manufacturer specification) and thickness ca. 50 μm. After activation and hydration, Nafion 1100 had a thickness of (63.7 ± 0.8) μm. After a completed permeation experiment, the membrane thickness was (64.9 ± 2.2) μm, suggesting insignificant swelling associated with sorption of methanol during the experiment. The water uptake of Nafion 1100 was (25 ± 2) % by mass, which is similar to literature reports of Nafion 117.[29] The solubility of methanol in Nafion 1100 was (0.31 ± 0.06). The thickness of membranes equilibrated in 1 M aqueous

methanol was within error of those equilibrated in DI water, further suggesting negligible membrane swelling during permeation experiments. As a control, the same methanol solubility measurement method was applied to Nafion 117, resulting in a methanol solubility of (0.50 ± 0.03), similar to previously reported literature values.[29,47,66] Table 2 presents the measured physical and transport properties of Nafion 1100 obtained in this work using at least 3 independent samples.

Table 2. The average measured physical and transport properties of Nafion 1100.

Property		Value	Units
Hydrated thickness	δ_m	63.7 ± 0.8	μm
Water uptake		25 ± 2	% mass
Methanol solubility coefficient	K_m	0.31 ± 0.06	
Mass transfer boundary layer thickness	δ_{BL}	4 ± 32	μm
Methanol diffusion coefficient	D_m	$(5.6 \pm 1) \times 10^{-6}$	cm^2/s
Methanol permeability	P_m	$(1.7 \pm 0.5) \times 10^{-6}$	cm^2/s

Experimental Mass Transfer Boundary Layer Thickness

The average mass transfer boundary layer thickness was estimated from experimental permeance and thickness data (included Table S3 in the SI) using Eqn. 11, and found to be (4 ± 32) μm. The uncertainty in the boundary layer was calculated from the propagation of the standard deviation in the permeance and membrane thickness calculated from multiple experiments (see SI pg 8).[53] Since a negative boundary layer thickness has no physical meaning, the realistic range for the mass transfer boundary layer thickness was between 0 and 36 μm. Using a boundary layer thickness of 4 μm, the diffusion coefficient was calculated from Eqn. 12 to be $((5.6 \pm 1.0) \times 10^{-6})$ cm^2/s, which is similar to literature values for Nafion 117.[28] In general, the diffusion coefficient of methanol is less than the diffusion coefficient of water in Nafion,[67] which has been reported in Nafion 115 to have a value of (9×10^{-6}) cm^2/s when the membrane is exposed to liquid water on one side and aqueous 4 M NaCl solution on the other.[68] Since one would expect the water diffusion coefficient to increase with decreasing salinity, the methanol diffusion coefficient measured herein is consistent with the literature value for the water diffusion coefficient.

The uncertainty is large relative to the thickness of the mass transfer boundary layer. Therefore it is important to consider how variation in the mass transfer boundary layer thickness would affect the calculation of the diffusion coefficient. Figure 2 presents the diffusion coefficient as a function of the mass transfer boundary layer thickness for an experimentally-measured permeance under the following conditions: $\mathbb{P}$ = $((2.7 \pm 0.1) \times 10^{-4})$ cm/s, δ_m= (63.9 ± 0.8) μm, K_m= (0.31± 0.06). Due to the uncertainty of the diffusion coefficient, a zero-thickness boundary layer and a 50 μm thick boundary layer are statistically indistinguishable.

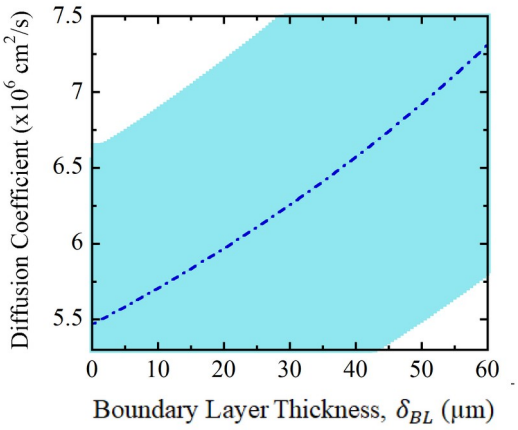

Figure 2. The diffusion coefficient calculated from Eqn. 12 for the conditions $\mathbb{P}$ = (2.7 ± 0.1) ×10^{-4} cm/s, δ_m= (63.9 ± 0.8) μm, K_m= (0.31± 0.06). The light blue region represents one standard deviation of the diffusion coefficient, calculated from the propagation of the standard deviations of the individual terms.

During these diffusion cell experiments, there is a water concentration gradient in the opposite direction of the methanol concentration gradient. Therefore, water flux could impact the observed concentration of methanol from which the diffusion coefficient is calculated. Calculations of the water flux in response to the concentration gradient across the membrane (i.e., osmotic flux) demonstrate that a maximum of 0.26 mL moves from the receiver to the donor cell and that any impacts of osmotic flux on the concentration of methanol is negligible (see Section 1 of the SI).

Experimental Determination of Permeability

The membrane permeability was calculated from Eqn. 1 using the mass transfer boundary layer thickness, the diffusion coefficient, and the solubility coefficient. The permeability of Nafion 1100 to methanol was ((1.7 ± 0.5) × 10^{-6}) cm^2/s. The Nafion 1100 membrane used here is similar in equivalent weight and thickness to the commercial Nafion 112 membrane, which has a reported methanol permeability coefficient ranging from (1.1 × 10^{-6}) to (2.5 ×10^{-6}) cm^2/s.[69,70] In thicker Nafion membranes of the same equivalent weight, the values of methanol permeability coefficient reported in the literature are in the range (1.2 × 10^{-6}) to (2.6 × 10^{-6}) cm^2/s.[37,47,71] Thus, the experimentally-determined methanol permeability coefficient of Nafion 1100 falls within the reported range for this material.

In the literature, permeability is commonly determined *via* Eqn. 7. When fitting Eqn. 7 to the experimental downstream concentration using P_m as a fitting parameter, we calculated an average permeability of ((1.76 ± 0.07) × 10^{-6}) cm^2/s. An example of the time-resolved methanol concentration measured in the downstream cell is presented in Figure 3 (Expt, black curve). Sensitivity studies of the fit to experimental data as well as data from replicate experiments are included in Fig. S5 and Fig. S6 of the SI. Included in Figure 3 is Eqn. 7 fit to the entire set of downstream concentration data. At time points beyond 1000 min, there appears to be a systematic difference between experiment and Eqn. 7. However, as can be seen immediately following the collection of new backgrounds (as designated by the grey dashed lines), the experimental results and Eqn. 7 are in much closer agreement. This suggests that the observed systematic difference between experimental data and Eqn. 7 at longer time points was the result of the FTIR instrument drift; this drift was mitigated by the collection of a new background but could not

be eliminated completely. The concentration predicted by Eqn. 7 supports the conservation of methanol mass.

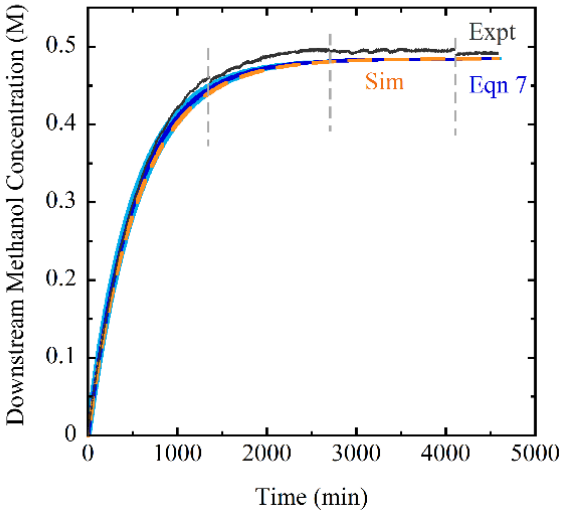

Figure 3. Time-resolved downstream cell methanol concentration for permeation through Nafion 1100: experimental results (black), the fit of Eqn. 7 to experimental data (blue), and simulation results (orange). Vertical dashed gray lines are the times at which a fresh background for the FTIR probe was collected. Error (light blue) associated with the fit of Eqn. 7 represents 1 standard deviation from the average P_m, which is barely larger than the linewidth.

Computational Fluid Dynamics Boundary Layer Thickness

The velocity magnitude, or speed, in the neck region (Fig. 1) is calculated to be 0.0005 - 0.012 m/s, significantly lower than the value of 0.03 - 0.1 in the bulk region, as shown in the speed profile of the upstream cell in Figure S7 of the SI. Figure 4a presents the speed and concentration profiles within 500 μm of the membrane surface. These profiles are the result of energy, momentum, and mass balances within the CFD simulation. Given that the concentration and hydrodynamic boundary layers are usually defined as the region in which concentration or speed is less than 99% of the bulk values,[56] the hydrodynamic boundary layer under the conditions of this study was greater than 500 μm and the concentration boundary layer on the order of 200 μm (Figure 4a). The methanol concentration (Figure S8 of the SI) was uniform in the bulk region of the upstream cell, indicating that the solution was well-mixed. Figure 4 shows the speed and concentration of methanol in the neck region near the membrane at 600 min after methanol had been added. The speed decreased continuously from its bulk value through the entire neck (4.8 mm) of the upstream cell. The decrease in concentration started 200 μm from the membrane.

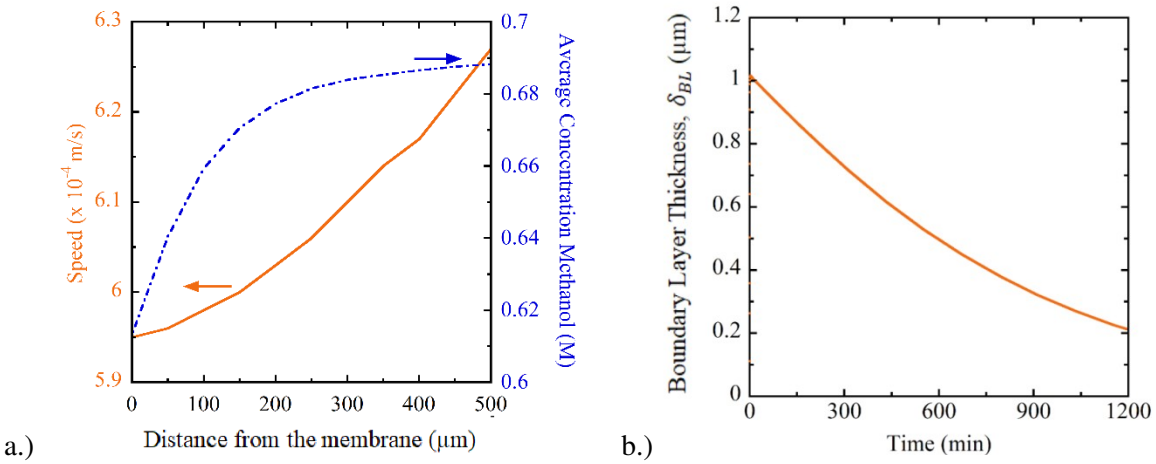

Figure 4. (a) The average speed of the solution and average concentration profile in the neck region of the upstream cell at t = 600 min. based on distance from the membrane. (b) The mass transfer boundary layer thickness, δ_{BL}, calculated from Eqn. 18 as a function of time.

The mass-transfer boundary layer thickness (Figure 4b) was determined from Eqn. 18 by idealizing the system into a well-mixed bulk region and a boundary layer region in which mass transport only occurs via diffusion. At the start of the simulation, when the methanol concentration was near 1 M, δ_{BL} was around 1 μm. Over time, the concentration gradient, and the related mass transfer coefficient decreased, until the concentrations in the upstream and downstream cells were equal. The boundary layer thickness computed at 1200 min was 0.2 μm, in agreement within experimental error to the value of δ_{BL} = 4 μm obtained from the measurements.

Multiscale Modeling Development

Simulations using the multiscale model described in the Methods section agree with the experimental data and the calculation using Eqn. 7 as shown in Figure 3. The agreement between the model and experiment suggests that the model includes the minimum set of mechanistic steps needed to describe permeation. These steps are adsorption, diffusion, and desorption of solutes from the membrane together with rapid transport of solutes between solution bulk and interface regions. The main distinction of this model from a continuum-level model is the explicit inclusion of adsorption and desorption as physical reactions at the membrane surface, which are fast relative to diffusion through the membrane, and only become rate-limiting if they are slowed by six or more orders of magnitude from their physically-relevant values. The good agreement between the simulation and experimental results indicate that treating methanol adsorption and desorption as reversible reactions at the interfaces is a valid method for describing the methanol phase change process in this system. The condition where the interfacial reactions become rate limiting provides an order of magnitude estimate for how severely transport to the membrane would have to be limited to affect the permeation measurements for this system.

The multiscale simulations provide a complete history of the system in space and time, which allows for examination of the methanol concentration in each region of the system. The concentrations in the bulk and interfacial membrane compartments were nearly identical at all times. They changed smoothly in the

bulk, C_s^b, and were slightly noisy in the interface C_s^n (Figure 5a). This is because at the interfaces, the methanol concentration, C_m^n, fluctuates (Figure 5b) due to adsorption and desorption processes. This result is physically realistic, and when averaged over time gives results consistent with the standard thermodynamically-based method in which the thermodynamic equilibrium $C_m^n = K_m \times C_s^n$ is valid at all time points. Finally, the gradient of C_m^n from the upstream to the downstream interface of the membrane is also noisy (Figure 5c), in contrast to the gradient calculated using the standard method. The dynamic nature of equilibrium is better highlighted by the stochastic algorithm solution, which shows that concentration gradients are zero on average but shift between positive and negative values over time; molecules move back and forth across the membrane at equilibrium, even though the net flux is zero.

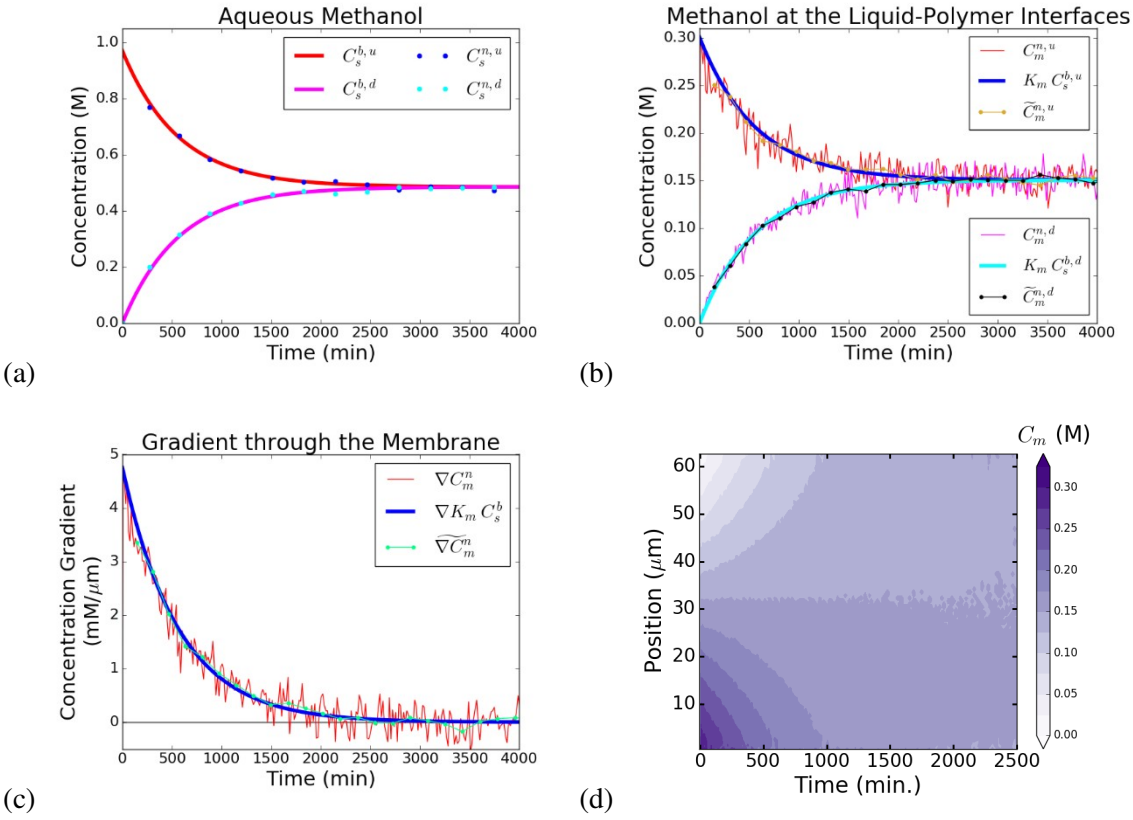

Figure 5. (a) Upstream and downstream aqueous methanol concentrations in the bulk and at the membrane surface over time. (b) Upstream and downstream concentration of methanol within the polymer in the interface regions. (c) The gradient for methanol across the polymer. (d) Contour plot of methanol concentration within the membrane versus time, in which the vertical axis shows the position in the membrane, where 0 is the upstream interface and 63 is the downstream interface; the light colors denote low concentration and darker colors denote higher concentration.

When membrane swelling was incorporated into the model, the membrane thickness increased by 0.643 μm, a change of only 1%, which occurred within the first 100 min. of the simulation. Even though the overall thickness did not increase further after 100 min., the microscopic picture was more complex: the

volumes of individual compartments continued to change as the methanol concentration changes, reaching a constant volume at 2500 min. The effect of membrane swelling on the time-resolved downstream methanol concentration was negligible in this case, indicating that swelling does not affect the permeability measurement in this system. This result is in contrast to our previous work on methanol sorption into Nafion, in which both swelling and diffusion were rate-limiting. The difference in the importance of swelling may be due to the way that the membranes were prepared prior to the measurements, and also to the differing time-scales of the experiments. Permeation takes place over relatively long time scales (thousands of minutes), whereas sorption/desorption takes place over relatively short time scales (minutes). Since swelling occurs on the 10-100 minute time-scale, the rate of swelling has a stronger effect on the sorption experiments, which take place on approximately the same time-scale.

Predictive Simulation of Methanol Permeation in a Solar-Driven CO_2 Reduction Device

Once a validated multiscale kinetic model for methanol permeation through Nafion was established, it was used to predict permeation in a solar-driven CO_2 reduction device. In these devices, sunlight produces a photovoltage that drives (photo)electrochemical conversion of carbon dioxide to liquid fuel products at the cathode and photoelectrochemical water splitting at the anode. The photovoltage is directly related to the intensity of the sunlight and consequently fluctuates throughout the day,[72,73] which affects the distribution of CO_2 reduction products.[34] The two electrodes are separated by aqueous electrolyte solutions and a polymer electrolyte membrane, as shown in Figure 6. Therefore, any liquid fuel product formed from the (photo)electrochemical conversion of carbon dioxide at the cathode generates a concentration gradient of the product across the membrane. As sunlight levels fluctuate, changes in product distribution and generation rates within the solar-fuels device alter the concentration to which the membrane is being exposed. Models that explicitly include molecular mechanisms of solute transport and transience in polymers are valuable to understand and predict membrane performance in these devices.

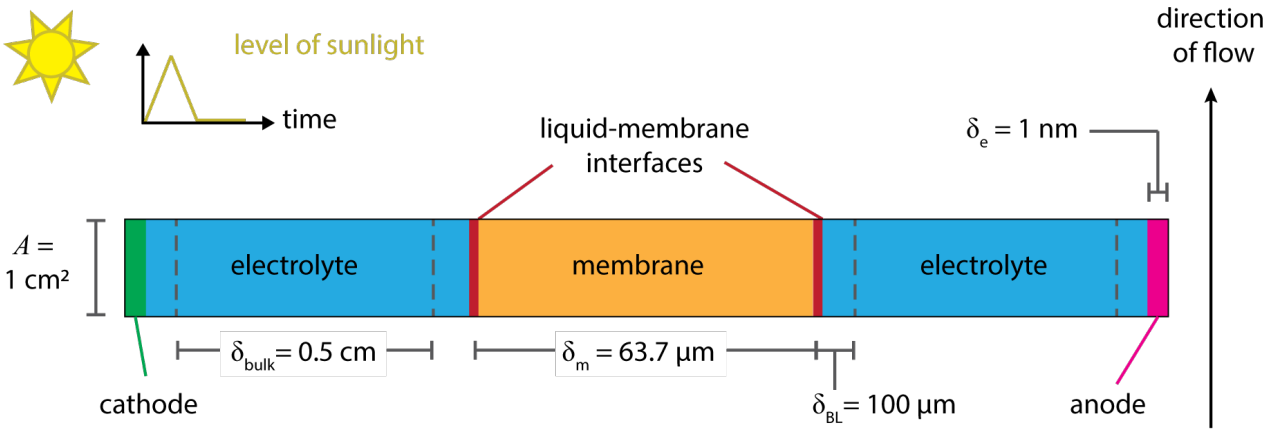

Figure 6. Diagram (not to scale) of a solar-driven CO_2 reduction device and setup for the multiscale model.

Here, we describe a predictive model of solar-driven CO_2-reduction device using the kinetic multiscale model for permeation established above. The mass transport steps in the bulk electrolyte and polymer membrane were treated as described above, as were the reversible adsorption and desorption reactions of methanol at the liquid-polymer interface. The 63.3 μm thick membrane was divided into 100 compartments; the membrane had the same D_m and K_m as listed in Table 2. In typical lab-scale devices, an electrode has a surface area of 1 cm^2, with the membrane area available for transport equal to the electrode area. The distance between the two electrodes is typically ~1 cm (shown in Fig. 6) The mass transfer boundary layer thickness in this unstirred device was unknown, and so a commonly assumed value of 100 μm (divided into 10 compartments) was used.[74]

The main difference between simulations of a methanol permeation experiment and the current simulations of a solar-driven CO_2 reduction device is the way in which methanol is introduced to the system. Here, there is no methanol at the start of the simulation; it is produced within the device based on the amount of sunlight. The production of methanol at the cathode (on the upstream side) was included using the reaction

$$\text{cathode} \xrightarrow{k'_{ECR}} \text{MeOH}_{(aq)} + \text{cathode} \qquad \text{Eqn. 22}$$

which maintains a constant concentration of cathode material. The rate coefficient, k'_{ECR}, was calculated as

$$k'_{ECR} = \chi(t)\, k_{ECR}\, C_{cathode} \qquad \text{Eqn. 23}$$

where $\chi(t)$ is the time-dependent normalized level of sunlight, k_{ECR} is the rate coefficient for electrochemical reduction (ECR) of CO_2 to methanol, and $C_{cathode}$ is the concentration of metal atoms upon which the ECR reaction can occur. Kuhl et al.[34] reported a current density of 0.02 mA/cm^2 at a potential of -1.14 V vs. RHE in a solution constantly saturated with dissolved CO_2 for this reaction on metallic copper surfaces. Metal sufaces typically have 10^{15} atoms/cm^2 of geometric surface area.[75] We assumed that the surface was rough and so was distributed over a 1 nm thickness, resulting in $C_{cathode} =$ 166 M. The conversion of CO_2 to MeOH consumes 6 electrons, so assuming that ECR and photo-electrochemical reduction have same current density, the current density was converted to the pseudo-zeroth order rate coefficient $k_{ECR}C_{cathode} =$ 2.07 M s^{-1}. The level of sunlight was assumed to follow a triangle wave, increasing from 0% to 100% over 4 h, then decreasing back to 0% over 4 h (see Fig. 6). The anode (on the downstream side) was assumed to be inert to methanol. so its oxidation rate was negligible.

One simulation was performed in which the bulk electrolyte solution was not circulated, i.e., there was mixing within the device only. A second simulation, in which the electrolyte flowed through the solution compartment at a rate of 5 mL/min,[29] removed the methanol from the device. Methanol removal from the solution was represented in the simulations using the following first-order reaction in the bulk solution regions,

$$\text{MeOH}_{(aq)} \xrightarrow{k_{out}} \text{MeOH}_{(out)} \qquad \text{Eqn. 24}$$

where k_{out} = 1.67 s^{-1} is the rate coefficient for methanol flowing out of the device (calculation in the SI).

In both simulations, methanol was produced only when sunlight was available (8 h), and the rate of production increased with the sunlight intensity. Since both simulations had the same sunlight conditions, they both produced the same total amount of methanol, (2.98×10^{-6}) moles. The time-dependent concentrations of methanol in different regions of the device were shown in Figure 7.

In the first simulation (Fig. 7a), the electrolyte remained within the device, resulting in methanol accumulation within the solution and the Nafion membrane. The maximum concentration of methanol, 2.92 mM, was reached at 7.4 h in the boundary layer closest to the cathode. As methanol was produced, it redistributed within the device, as the system moved towards equilibrium. The bulk concentration of methanol reached 1.46 mM (half-way to the equilibrium value) at 3.7 h in the catholyte and at 4.3 h in the anolyte, indicating a lag of 0.6 h between the two sides of the device reaching the same concentration. At 9.4 h, the device reached equilibrium where the spatial distribution of methanol throughout the system was constant. Within the membrane, the methanol concentration at equilibrium was ((9 ± 1) $\times 10^{-4}$) M, much lower than that for the permeation experiments.

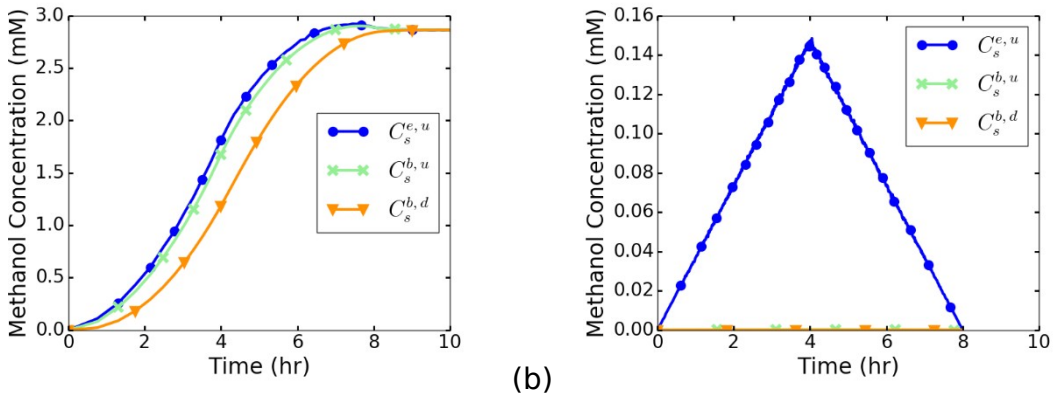

Figure 7. Time-dependent methanol concentrations within a solar-driven CO_2 reduction device (a) without flow and (b) with flow. The blue dots are for the solution within the boundary layer next to the cathode, $C_s^{e,u}$. The green x's are for the upstream bulk, $C_s^{b,u}$. The orange triangles are for the downstream bulk, $C_s^{b,d}$. Note that the vertical axes are not on the same scale.

In the second simulation (Fig. 7b), the electrolyte was circulated so that methanol was removed from the device. In this situation, the maximum concentration of methanol was (1.48×10^{-4}) M in the boundary layer closest to the cathode, a value reached at 4 h, the point of maximum methanol production rate. The concentration of methanol in the catholyte bulk solution peaked at (2.78×10^{-7}) M, also at 4 h. The flow of electrolyte on the upstream side removed most of the methanol before it reached the membrane, thereby keeping the concentration of methanol in the bulk electrolyte solution low. The maximum concentration of methanol within the membrane only reached (5.21×10^{-7}) M. Even for a membrane more easily affected by methanol than Nafion, the low concentration exposure here indicated that methanol-

induced changes to polymer structure and permeability within a solar fuels device would only occur *via* long term processes. More detailed information on time- and position-dependent methanol concentrations in these two predictive simulations was provided in the SI (Figs. S13 and S14).

The electrolyte flow rate used herein is on the low end of what is typical in these devices,[76–78] and so real devices are expected to have similar or better methanol recovery than predicted. In total, it was predicted that (2.98×10^{-6}) moles would be collected from the upstream (cathode) side, which is >99% recovery, assuming that efficient separation from water is possible. A very small fraction of methanol, (6.49×10^{-10}) moles or 0.02%, crossed over to the downstream side. The transport coefficient that controls the rate of mixing within the electrolyte solution was both increased and decreased by an order of magnitude with no change in the recovery of methanol, indicating that the simulations were insensitive to this value.

Furthermore, the same amount of methanol was recovered when a thinner δ_{BL} of 10 μm was tested.

Despite the high recovery, the circulation of the electrolyte had a disadvantage in that the CO_2 reduction products became very diluted. In the case of a 5 mL/min flowrate, 2.4 L of electrolyte flows through the upstream side of the device during the 8 h of sunlight, resulting in a methanol concentration within the collected electrolyte of only (1.24×10^{-6}) M. Separations to recover such low concentrations would be energetically expensive.[79]

DISCUSSION

Knowledge of the permeability of solutes through membranes is critical to enable the prediction of performance for devices involving membrane separators. We have developed a method to determine membrane permeability from quantitative measurements and calculations, and have demonstrated it for methanol permeation through Nafion using a diffusion cell. The multiscale kinetic model validated in this work offers insight into the key mechanistic processes and the rate-determining steps that control methanol permeation through Nafion under the conditions studied.

The method does not assume that ideal conditions – absence of swelling and boundary layers, and stable permeability – are present, rather, it assesses each in turn. Time-resolved concentration data are key to this process, and it is essential to be confident in their accuracy. As described in the Experimental Development section, we were able to identify and implement three improvements to the experimental methodology described previously[32,47] – eliminating gas bubble formation, adjusting for instrument drift, and utilizing a two-point baseline during data analysis – that enable a closing of the mass balance within 0.005 g methanol across the more than 3 days duration of the experiment (Figure S4 of the SI). A closed mass balance supports confidence in the accuracy of the time-resolved downstream concentration profile as measured using infrared spectroscopy. These improvements primarily affect the measurement of the upstream concentration at early times, as well as the measurement of concentration on both sides of the membrane over the extended periods of time required to reach full equilibration.

The most complex element to assess is whether interfacial boundary layers between the membrane and the bulk solution are present, as they may significantly complicate the calculation of the membrane permeability. If Eqn. 7 alone is used to calculate permeability, the resulting value would be a space-average of the permeability through both boundary layers and the membrane. The presence of a boundary layer is evaluated using two independent methods, permeance measurements, and CFD calculations. In the permeance measurement, the mass transfer boundary layer represents resistance to mass transport

between the two bulk solutions and the membrane and is the boundary layer of interest. Its thickness is determined using measurements for two different membrane thicknesses. The concentration and velocity profiles characterized using the CFD calculations contribute in a complex manner to the mass transfer boundary layer. It is important to understand how the concentration boundary layer impacts the calculation of the membrane permeability, as this specifically related to condition (ii) required by Eqn. 7. From the CFD simulations (Fig. 4), there is a methanol concentration difference between the bulk solution and the interface of at least 0.08 M at 600 min. This raises the question of whether condition (ii) is in fact met. If not, using Eqn. 7 will result an inaccurate membrane permeability. To check, we use Eqn. 7 to fit the experimental data directly and calculate a permeability of $((1.76 \pm 0.07) \times 10^{-6})$ cm^2/s. This value is within the uncertainty of the permeability calculation using Eqn. 12, which includes the presence of boundary layers. The agreement between the two values suggests that the concentration difference between the bulk and the interface solution regions determined by CFD is insignificant for the conditions and material used. That boundary layers do not affect the measurements cannot be assumed *a priori*, it must be specifically tested for the permeation cell in use.

There is one other criterion, condition (iii), that must be met in order for Eqn. 7 to be valid for calculation of a membrane permeability. To assess this point, we fit Eqn. 7 to different time periods within the same experimental run. Based on a two-sample t-test, there is no significant difference in the permeability calculated from data collected in the first 200 min (1.73×10^{-6} cm^2/s) and the permeability calculated from the entire 3000 min (1.76×10^{-6} cm^2/s). experiment, suggesting that the membrane permeability is constant with time.

Taken together, the measurements and calculations show that for this specific set of conditions for methanol permeation through Nafion, the use of Eqn. 7 is satisfactory for the determination of the membrane's permeability. We suggest that this system could be useful as a benchmark for measurements of permeability in other membrane-permeant combinations and permeation cell architectures. If the concentration vs time data reported here are reproduced, it is likely that interference from boundary layers is minimal and that the membrane's properties are constant.

We show in this work that a multiscale model for permeation using a kinetic (reaction-diffusion) framework, validated by the measurements, is an alternative to continuum-level expressions derived from the solution-diffusion model, such as Eqn. 7. Under simple conditions, the results of the multiscale simulations, the solution-diffusion-based model, and experiment are all consistent. However, if additional phenomena, e.g., swelling, are occurring, then fitting the experimental results with the solution-diffusion-based model does not reflect the true physics of the permeation process,[28] and it can be difficult to assess which mechanistic step is causing the discrepancy. The multiscale simulations allow us to investigate the effects of each mechanistic step in isolation. The primary mechanistic steps of the two models are similar, i.e., adsorption at the upstream interface, diffusion through the membrane, and desorption at the downstream interface. We show, however, that in contrast to the continuum-level solution-diffusion model, the mechanistic model must use reversible physical reactions (Eqn. 19) for the adsorption and desorption steps in order for the correct downstream time-resolved methanol concentration to be predicted. It is therefore a more complete description of permeation and more general. The use of a reversible reaction highlights the fact that adsorption and desorption are net processes, the consequence of slight imbalances in the instantaneous rates of forward (adsorption) and reverse (desorption) reactions at the interfaces. The reactions at the aqueous methanol – Nafion interface are fast compared to diffusion through the membrane, which is why the standard modeling assumption of thermodynamic equilibrium at

the interface (i.e., $C_m^n = K_m \times C_s^n$) works well at all time points even when the system as a whole is far from equilibrium. Once the system has reached equilibrium, the reversible adsorption and desorption reactions continue to occur, but their rates are equal such that the same average methanol concentrations within each phase (i.e., solution or membrane) are maintained. Diffusion also continues at equilibrium, with flux driven by fluctuations in the local concentration gradients, but the net effects of forward and backward diffusion cancel out.

A multiscale model is particularly useful for predicting permeability in other architectures or reacting systems that use the same materials. In the present work we compare the results of production of methanol in a solar-driven device for one diurnal cycle with and without electrolyte recirculation, and show that this one process element has a marked effect on the efficiency of product recovery as well as on the chemical environment experienced by the membrane in use. Moreover, the multiscale model adds flexibility to standard solution-diffusion modeling, because it can predict permeation under non-ideal conditions where an analytical model may be expected to perform poorly. Non-ideal conditions are those where any of conditions (i) - (iii) are not met, for example polymers that swell during permeation (discussed in the Results section and in more detail in section 3 of the SI), and polymers that undergo changes in permeability, for example in stimuli-responsive polymers.[80,81]

CONCLUSIONS

This study pursues an accurate understanding of the mechanisms of membrane permeability, which would enable prediction of material performance in applications and contexts different from those under which they were measured in the laboratory. Herein, a rigorous experimental method and analysis of experimental data has established the permeability of methanol through Nafion under conditions where the mass transfer boundary layer is 4 μm thick. Rigorous control of experimental conditions is used to produce a data set of high accuracy, which is then analyzed in two ways: (i) calculation of membrane permeance, which involves minimal assumptions, and (ii) fitting to Eqn. 7, which has a set of assumptions built in. These highly accurate experimental data are also used to validate a multiscale model in order to obtain a better picture of the physical mechanisms of permeation. This model includes adsorption, diffusion, and desorption of methanol from the membrane and identifies the absorption and desorption steps at the interface as rapidly-maintained equilibria. In addition, the multiscale model developed herein provides a viable route to determining permeability under transient conditions, for example in cases of polymer swelling and as is relevant to solar fuel devices. This strategy of experimental method, analysis, and simulation is broadly applicable to many types of polymer membranes.

ACKNOWLEDGEMENTS

This material is based upon work performed at the Joint Center for Artificial Photosynthesis, a DOE Energy Innovation Hub, supported through the Office of Science of the U.S. Department of Energy under Award Number DE-SC0004993.

NOMENCLATURE

For concentrations, the following nomenclature is used:

$$C_{phase}^{location\ within\ the\ cell,\ \ location\ within\ system}$$

where the phase is either the membrane phase (*m*) or the solution phase (*s*), the location within the the cell is either the bulk (*b*) or the membrane-solution interface (*n*), and the location within the system is either upstream (*u*) or downstream (*d*). Thicknesses are distinguished with *m* for membrane and *BL* for the boundary layer.

Value	Variable	Units (unless otherwise specified)
Permeability	P	cm^2/s
Solubility coefficient	K	
Diffusion coefficient	D	cm^2/s
Concentration	C	mol/L
Mass flux	J	$kg/cm^2\ s$
Thickness	δ	μm
Time	t	min
Active area for transport	A	cm^2
Volume	V	mL
Resistance	R	s/cm
Permeance	$\mathbb{P}$	cm/s
Velocity profile	$\mathbf{u}$	m/s
Density	ρ	kg/m^2
Dynamic viscocity	μ	Pa s
Pressure	p	Pa
Rate coefficient	k	s^{-1}

REFERENCES

1. Staffell, I., Scamman, D., Velazquez Abad, A., Balcombe, P., Dodds, P. E., Ekins, P., Shah, N., Ward, K. R. *Energy Environ. Sci.*, 2019, **12**, 463–491.

2. Gür, T. M. *Energy Environ. Sci.*, 2018, **11**, 2696–2767.

3. Michl, J. *Nat. Chem.*, 2011, **3**, 268–269.

4. Montoya, J. H., Seitz, L. C., Chakthranont, P., Vojvodic, A., Jaramillo, T. F., Nørskov, J. K. *Nat. Mater.*, 2016, **16**, 70–81.

5. Zhang, L., Liu, R.-S., Liu, H., Sun, A., Zhang, J. Electrochemical Technologies for Energy Storage and Conversion, Wiley, 1st Ed., 2012.

6. Fuller, T. F., Harb, J. N. Electrochemical Engineering, John Wiley & Sons, Inc., 1st Ed., 2018.

7. Singh, M. R., Bell, A. T. *Energy Environ. Sci.*, 2016, **9**, 193–199.

8. Jin, J., Walczak, K., Singh, M. R., Karp, C., Lewis, N. S., Xiang, C. *Energy Environ. Sci.*, 2014, **7**, 3371–3380.

9. Zhao, T. S., Xu, C., Chen, R., Yang, W. W. *Prog. Energy Combust. Sci.*, 2009, **35**, 275–292.

10. Luo, T., Abdu, S., Wessling, M. *J. Membr. Sci.*, 2018, **555**, 429–454.

11. Wang, C. Y. *Chem. Rev.*, 2004, **104**, 4727–4765.

12. Kamcev, J., Freeman, B. D. *Annu. Rev. Chem. Biomol. Eng.*, 2016, **7**, 111–133.

13. Varcoe, J. R., Atanassov, P., Dekel, D. R., Herring, A. M., Hickner, M. A., Kohl, P. A., Kucernak, A. R., Mustain, W. E., Nijmeijer, K., Scott, K., Xu, T., Zhuang, L. *Energy Environ. Sci.*, 2014, **7**, 3135–3191.

14. Maurya, S., Shin, S. H., Kim, Y., Moon, S. H. *RSC Adv.*, 2015, **5**, 37206–37230.

15. Peighambardoust, S. J., Rowshanzamir, S., Amjadi, M. *Int. J. Hydrogen Energy*, 2010, **35**, 9349–9384.

16. Baker, R. W. Membrane Technology and Applications, John Wiley & Sons, Ltd, 3rd Ed., 2012.

17. Wijmans, J. G., Baker, R. W. *J. Membr. Sci.*, 1995, **107**, 1–21.

18. Geise, G. M., Paul, D. R., Freeman, B. D. *Prog. Polym. Sci.*, 2014, **39**, 1–24.

19. Kamcev, J., Paul, D. R., Manning, G. S., Freeman, B. D. *ACS Appl. Mater. Interfaces*, 2017, **9**, 4044–4056.

20. Petropoulos, J., Sanopoulou, M., Papadokostaki, K. *Diffus. Fundam.*, 2009, **11**, 1–2.

21. Pönitsch, M., Kirchheim, R. *Scr. Mater.*, 1996, **34**, 1479–1482.

22. Hofmann, D., Fritz, L., Ulbrich, J., Paul, D. *Comput. Theor. Polym. Sci.*, 2000, **10**, 419–436.

23. Hofmann, D., Fritz, L., Ulbrich, J., Schepers, C., Bhning, M. *Macromol. Theory Simulations*, 2000, **9**, 293–327.

24. Hofmann, D., Heuchel, M., Yampolskii, Y., Khotimskii, V., Shantarovich, V. *Macromolecules*, 2002, **35**, 2129–2140.

25. Hölck, O., Siegert, M. R., Heuchel, M., Böhning, M. *Macromolecules*, 2006, **39**, 9590–9604.

26. Soniat, M., Tesfaye, M., Brooks, D., Merinov, B., Goddard, W. A., Weber, A., Houle, F. A. *Polymer*, 2018, **134**, 125–142.

27. Soniat, M., Tesfaye, M., Mafi, A., Brooks, D. J., Humphrey, N. D., Weng, L.-C., Merinov, B., Goddard, William A., I., Weber, A. Z., Houle, F. A. *J. Polym. Sci.*, 2020, **58**, 1207–1228.

28. Soniat, M., Houle, F. A. *J. Phys. Chem. B*, 2018, **122**, 8255–8268.

29. Hallinan, D. T., Elabd, Y. A. *J. Phys. Chem. B*, 2007, **111**, 13221–13230.

30. Yasuda, H., Lamaze, C. E., Ikenberry, L. D. *Die Makromol. Chemie*, 1968, **118**, 19–35.

31. Geise, G. M., Freeman, B. D., Paul, D. R. *Polymer*, 2010, **51**, 5815–5822.

32. Carter, B. M., Dobyns, B. M., Beckingham, B. S., Miller, D. J. *Polym.*, 2017, **123**, 144–152.

33. Kamcev, J., Doherty, C. M., Lopez, K. P., Hill, A. J., Paul, D. R., Freeman, B. D. *J. Membr. Sci.*, 2018, **566**, 307–316.

34. Kuhl, K. P., Cave, E. R., Abram, D. N., Jaramillo, T. F. *Energy Environ. Sci.*, 2012, **5**, 7050–7059.

35. Galizia, M., Paul, D. R., Freeman, B. D. *Polymer*, 2016, **102**, 281–291.

36. Malmali, M., Stickel, J. J., Wickramasinghe, S. R. *Sep. Purif. Technol.*, 2014, **132**, 655–665.

37. Varcoe, J. R., Slade, R. C. T., Yee, E. L. H., Poynton, S. D., Driscoll, D. J. *J. Power Sources*, 2007, **173**, 194–199.

38. Langergraber, G., Fleischmann, N., Hofstädter, F. *Water Sci. Technol.*, 2003, **47**, 63–71.

39. Johnson, K. S., Coletti, L. J. *Deep. Res. Part I Oceanogr. Res. Pap.*, 2002, **49**, 1291–1305.

40. Hartig, D., Hacke, S., Scholl, S. *Chem. Eng. Technol.*, 2018, **41**, 454–460.

41. Freger, V., Korin, E., Wisniak, J., Korngold, E. *J. Membr. Sci.*, 1997, **128**, 255–267.

42. Freger, V., Korin, E., Wisniak, J., Korngold, E. *J. Membr. Sci.*, 2000, **164**, 251–256.

43. Flynn, G. L., French, A. B., Ho, N. F. H., Higuchi, W. I., Ostafin, E. A., Warbasse, L. H., Amidon, G. E., Williams, E. *J. Membr. Sci.*, 1984, **19**, 289–308.

44. Derlacki, Z. J., Easteal, A. J., Edge, A. V. J., Woolf, L. A., Roksandic, Z. *J. Phys. Chem.*, 1985, **89**, 5318–5322.

45. Technical Information Data Sheet for Nafion PFSA Products. *DuPont*, 2002

46. Rhee, Y. W., Ha, S. Y., Masel, R. I. *J. Power Sources*, 2003, **117**, 35–38.

47. Beckingham, B. S., Lynd, N. A., Miller, D. J. *J. Membr. Sci.*, 2018, **550**, 348–356.

48. Cussler, E. L. Diffusion: Mass Transfer in Fluid Systems, Cambridge University Press, New York, 2nd Ed., 2003.

49. Plyler, E. K. *J. Res. Natl. Bur. Stand.*, 1952, **48**, 281–286.

50. iC IR Software, v. 7.1.84, Mettler-Toledo AutoChem, Inc., 2018

51. MacBride, D. M., Malone, C. G., Hebb, J. P., Cravalho, E. G. *Appl. Spectrosc.*, 1997, **51**, 43–50.

52. Bakalyar, S. R., Bradley, M. P. T., Honganen, R. *J. Chromatogr.*, 1978, **158**, 277–293.

53. Harris, D. C. Quantitative Chemical Analysis, W. H. Freeman and Company, New York, 6th Ed., 2003.

54. COMSOL Multiphysics Software, v. 5.4, COMSOL AB, Stolkholm Sweden

55. CFD Module User's Guide, COMSOL AB, Stockholm, Sweden, COMSOL Mul., 2018.

56. Welty, W., Rorrer, W. Fundamentals of Momentum, Heat, and Mass Transer, John Wiley & Sons, Inc., 4th Ed., 2001.

57. Bunker, D. L. *Acc. Chem. Res.*, 1974, **7**, 195–201.

58. Young, S., Trevino, S., Tan, N. *J. Polym. Sci. Part B Polym. Phys.*, 2002, **40**, 387–400.

59. Yi, Y., Bae, Y. *Polymer*, 2017, **130**, 112–123.

60. Peters, B. Reaction Rate Theory and Rare Events, Elseveir, Amsterdam, Netherlands, 2017.

61. Hinsberg, WD and Houle, FA, Kinetiscope, available at www.hinsberg.net/kinetiscope, accessed August 2020

62. Bunker, D. L., Garrett, B., Kleindienst, T., Long, G. S. *Combust. Flame*, 1974, **23**, 373–379.

63. Gillespie, D. T. *J. Comput. Phys.*, 1976, **22**, 403–434.

64. Houle, F. a., Hinsberg, W. D., Morrison, M., Sanchez, M. I., Wallraff, G., Larson, C., Hoffnagle, J. *J. Vac. Sci. Technol. B Microelectron. Nanom. Struct.*, 2000, **18**, 1874.

65. Gillespie, D. T. *Annu. Rev. Phys. Chem.*, 2007, **58**, 35–55.

66. Ren, X., Springer, T. E., Zawodzinski, T. A., Gottesfeld, S. *Fuel Cells*, 2000, **147**, 466–474.

67. Kusoglu, A., Weber, A. Z. *Chem. Rev.*, 2017, **117**, 987–1104.

68. Kingsbury, R. S., Zhu, S., Flotron, S., Coronell, O. *ACS Appl. Mater. Interfaces*, 2018, **10**, 39745–39756.

69. Neves, L. A., Coelhoso, I. M., Crespo, J. G. *J. Membr. Sci.*, 2010, **360**, 363–370.

70. Wen, S., Gong, C., Tsen, W.-C., Shu, Y.-C., Tsai, F.-C. *J. Appl. Polym. Sci.*, 2010, **116**, 1491–1498.

71. Tricoli, V., Carretta, N., Bartolozzi, M. *J. Electrochem. Soc.*, 2002, **147**, 1286.

72. Chen, Y., Lewis, N. S., Xiang, C. *ACS Energy Lett.*, 2016, **1**, 273–280.

73. Stevens, J. C., Weber, A. Z. *J. Electrochem. Soc.*, 2016, **163**, H475–H484.

74. Singh, M. R., Clark, E. L., Bell, A. T. *Phys. Chem. Chem. Phys.*, 2015, **17**, 18924–18936.

75. Somorjai, G. A., Li, Y. Introduction to Surface Chemistry and Catalysis, Wiley, Inc., 2010.

76. Yang, H., Kaczur, J. J., Sajjad, S. D., Masel, R. I. *J. CO2 Util.*, 2017, **20**, 208–217.

77. Sullivan, I. Personal Communication, August 2020

78. Sullivan, I., Han, L., Lee, S. H., Lin, M., Larson, D. M., Drisdell, W. S., Xiang, C. *ACS Sustain. Chem. Eng.*, 2019, **7**, 16964–16970.

79. Greenblatt, J. B., Miller, D. J., Ager, J. W., Houle, F. A., Sharp, I. D. *Joule*, 2018, **2**, 381–420.

80. Geismann, C., Yaroshchuk, A., Ulbricht, M. *Langmuir*, 2007, **23**, 76–83.

81. Kim, K. T., Cornelissen, J. J. L. M., Nolte, R. J. M., Van Hest, J. C. M. *Adv. Mater.*, 2009, **21**, 2787–2791.